

# How do galactic winds affect the Ly $\alpha$ forest?

Serena Bertone<sup>1,2\*</sup> and Simon D.M. White<sup>2</sup>

<sup>1</sup>*Astronomy Centre, University of Sussex, Brighton BN1 9QH, United Kingdom*

<sup>2</sup>*Max Planck Institut für Astrophysik, Karl Schwarzschild Str. 1, 85741 Garching bei München, Germany*

Submitted to MNRAS

## ABSTRACT

We investigate the effect of galactic winds on the Ly $\alpha$  forest in cosmological simulations of structure and galaxy formation. We combine high resolution N-body simulations for the evolution of the dark matter with a semi-analytic model for the formation and evolution of galaxies which includes detailed prescriptions for the long-term evolution of galactic winds. We find that the main statistical properties of the Ly $\alpha$  forest, namely the power spectrum  $P(k)$  and the flux probability distribution function (PDF), are not significantly affected by winds and do not give a unique answer when trying to rule out or constrain wind models. Winds expanding around galaxies do, however, produce detectable signatures in the forest, in the form of increased flux transmissivity inside hot bubbles and narrow, saturated absorption lines corresponding to dense cooled shells. We find that the Ly $\alpha$  flux transmissivity is highly enhanced in proximity of wind-blowing galaxies, which represent up to half the galaxies in our sample, in agreement with the results of Adelberger et al. 2005. We finally propose a new method to test for the presence of absorption lines due to wind shells in the Ly $\alpha$  forest: we calculate the number distribution of saturated regions in spectra as a function of their width and we find that the number of saturated regions with widths smaller than about 1 Å at  $z = 3$  and 0.6 Å at  $z = 2$  may be more than doubled. This effect should be clearly detectable in real spectra.

**Key words:** cosmology: theory – intergalactic medium – quasars: absorption lines

## 1 INTRODUCTION

Extensive observations of QSO spectra have provided a wealth of information on properties of the intergalactic medium (IGM).

The Ly $\alpha$  forest provides a measure of the power spectrum of density fluctuations  $P_m(k)$  on smaller scales than those accessible by Cosmic Microwave Background (CMB) observations (Spergel et al. 2003, Viel et al. 2004a) or large-scale structure surveys (e.g. Tegmark et al. 2004, Viana, Nichol & Liddle 2002, Colless et al. 2001). The flux power spectrum  $P(k)$  of the Ly $\alpha$  forest is directly related to the power spectrum of density fluctuations  $P_m(k)$ , thanks to the existence of a direct connection between the Ly $\alpha$  absorption and the underlying density and velocity fields (Viel et al. 2004b, Croft et al. 2002, Hui et al. 2001, Croft et al. 1998). The flux power spectrum  $P(k)$  has been estimated at redshifts  $1 < z < 4$  (Kim et al. 2004, McDonald et al. 2004, Croft et al. 2002, McDonald et al. 2000, Croft et al. 1998) for  $0.001 < k < 0.1 \text{ s km}^{-1}$ , corresponding to scales of up to about  $50 h^{-1}$  comoving Mpc. Given that the data sets used by different groups were taken with different in-

struments (e.g. UVES, HIRES, LRIS) on different telescopes (e.g. VLT, Keck, SDSS Apache Point) and at different resolution and signal-to-noise ratio, the agreement between the results is spectacular.

When using the matter power spectrum  $P_m(k)$  from the Ly $\alpha$  forest to estimate cosmological parameters in conjunction with CMB and large-scale structure data sets, it is important to know precisely how  $P(k)$  is affected by sources of systematic errors and non-cosmological distortions. For example, the estimation of the unabsorbed continuum level in a QSO spectrum is extremely sensitive to fluctuations in the cosmic UV background radiation, which is poorly constrained, and this affects both the amplitude and slope of  $P(k)$  (Lidz et al. 2005, McDonald et al. 2005, Viel et al. 2004c, Hui et al. 2001). High column density absorbers with damping wings and signatures of galactic winds may produce “local” distortions in the Ly $\alpha$  forest which introduce deviations in the power spectrum at smaller scales (Fang et al. 2005, McDonald et al. 2005, Viel et al. 2004c). The presence of metal lines blended with the Ly $\alpha$  forest affects the flux power spectrum at very small scales (Kim et al. 2004).

Adelberger et al. (2003) jointly analysed high resolution quasar spectra and spectra of Lyman break galaxies (LBG) near the quasar lines-of-sight. Their earliest results indi-

\* E-mail: s.bertone@sussex.ac.uk

cated that the Ly $\alpha$  continuum emitted by the background quasars can be almost completely transmitted by the intergalactic medium (IGM) near LBGs. Numerical simulations (Desjacques et al. 2004, Maselli et al. 2004, Kollmeier et al. 2003) have been unable to reproduce this result, predicting instead a decrease in the Ly $\alpha$  flux transmissivity with decreasing impact parameter (the impact parameter is defined as the minimum distance between a galaxy and the quasar line-of-sight). When new results derived from a larger observational sample were released (Adelberger et al. 2005, hereafter A05), the improved statistics showed that the mean transmitted flux around LBG does indeed decrease with decreasing impact parameter, as predicted by the simulations, but about a third of the galaxies in the full sample still show little or no Ly $\alpha$  absorption in their proximity. This suggests that the earlier result of Adelberger et al. (2003) was affected by small number statistics, although even a relatively small fraction of LBG’s “bubbles” in absorption appears inconsistent with published simulations.

In this work, we use a semi-analytic model for the long-term evolution of galactic winds by Bertone, Stoehr & White (2005, BSW05 hereafter) to investigate the effect of galactic winds on the Ly $\alpha$  forest. In particular, we calculate the flux probability distribution function (PDF), the flux power spectrum  $P(k)$  and the Ly $\alpha$  flux transmissivity near high redshift galaxies, and we compare the numerical results with the relevant observations. We consider three different models, a “no wind” model and two wind models corresponding to qualitatively different scenarios, and we try to determine which model better reproduces the observations. In addition, the comparison of the “no wind” model with the two wind models highlights the effects of galactic winds on the Ly $\alpha$  forest. To do this, we extract artificial spectra from the “M3” set of high resolution N-body simulations (Stoehr 2003), which combines a large dynamical range with a high mass resolution. The semi-analytic wind model of BSW05 includes a new description of the dynamics of the winds as a two-phase process: a first phase of adiabatic evolution during which the gas outflowing from galaxies is hot, and a second snowplough phase in which the wind material cools down and accumulates in a thin shell pushed by the momentum of the wind. The efficiency of winds in the simulations is set by a parameter ( $\varepsilon$ , see Subsection 2.2) that determines the amount of mass swept up by the expanding gas.

The paper is organised as follows. In Section 2 we briefly describe our set of simulations and the semi-analytic model for winds of BSW05. Section 3 presents our method to extract artificial spectra from the simulations and to include the contributions of winds. Detailed descriptions of our calculation of the hydrogen ionisation state and of the flux spectrum are given in Appendix A and Appendix B respectively. Results are presented in Section 4 for the flux PDF and in Section 5 for the power spectrum. In Section 6 we present our results for the flux transmissivity around LBG and we discuss the observations of A05. In Section 7 we present a new method to test statistically for the signature of winds in spectra and we conclude in Section 8.

## 2 SEMI-ANALYTIC SIMULATIONS OF GALACTIC WINDS

Since we want to investigate the effects of outflows in their proper cosmological context, we opt for a combination of N-body simulations for the evolution of the dark matter density field and a semi-analytic model for the formation and evolution of galaxies. This choice gives us the possibility to efficiently combine a high resolution in mass with a large simulated volume, as is necessary to study the effects of feedback from galaxies with a wide range in stellar mass. The large volume allows us to achieve a good statistics when investigating the effect of different galaxy populations on their surroundings. Our simulations assume a  $\Lambda$ CDM cosmology with matter density  $\Omega_m = 0.3$ , dark energy density  $\Omega_\Lambda = 0.7$ , Hubble constant  $h = 0.7$ , primordial spectral index  $n = 1$  and normalisation  $\sigma_8 = 0.9$ .

In the following subsections we briefly describe our set of numerical simulations (Subsection 2.1) and our semi-analytic model for the physics of galactic winds (Subsection 2.2). However, for a more detailed description of the wind model, we refer the interested reader to BSW05.

### 2.1 The M3 simulations

We use the “M3” high-resolution N-body simulation of Stoehr (2003). M3 is a resimulation at higher resolution of an approximately spherical region of the universe with average density close to the cosmic mean and diameter 52  $h^{-1}$  Mpc. The particle mass in the high resolution region is  $1.7 \cdot 10^8 h^{-1} M_\odot$  and the number of particles about  $7 \cdot 10^7$ . The simulations were performed using the parallel treecode GADGET I (Springel et al. 2001a) and 52 simulation outputs were stored between  $z = 20$  and  $z = 0$ .

The formation and evolution of galaxies is modelled with the semi-analytic technique of Springel et al. (2001b). Merging trees extracted from the simulations are used to follow the galaxy population in time, while simple prescriptions for gas cooling, star formation and galaxy merging model the processes involving the baryonic component of the galaxies. At  $z = 3$  a total of about four hundred thousand galaxies are identified and about three hundred and fifty thousand are present at  $z = 0$ . About half of the galaxies at  $z = 0$  are field galaxies, while the rest are in groups and poor clusters. The two largest clusters have a total mass of about  $10^{14} h^{-1} M_\odot$ . The recipes for the evolution of winds are implemented on top of this pre-existing scheme.

### 2.2 The wind model

BSW05 introduced new prescriptions for the evolution of galactic winds in the semi-analytic model for galaxy formation of Springel et al. (2001b). The most innovative feature of their prescriptions is a description of the dynamics of outflows as a two-phase process: a pressure-driven adiabatic expansion followed by a momentum-driven snowplough.

We do not resolve the first phases of the wind evolution, when a superbubble sweeps through the ISM of a galaxy. Instead, we follow the long-term evolution of winds once they have escaped the visible regions of galaxies. We make the simplifying assumption of spherical symmetry for the wind evolution. This may seem a rough approximation at

$z \sim 0$ , where outflows are mostly bipolar, but it is a good assumption at higher redshifts, where outflows seem to have a more spherical geometry (Shapley et al. 2003, Rupke et al. 2005).

Galactic winds are modelled as uniform pressure-driven bubbles of hot gas emerging from star-forming galaxies. The assumption that winds are adiabatic at blow-out is motivated by observations of galaxies in the local universe. For example, Hoopes et al. (2003) and Strickland & Stevens (2000) observe no energy losses in M82 through radiative cooling of the coronal ( $T \sim 10^{5.5}$  K) and the hot ( $T \sim 10^7$  K) phases of the wind, supporting the idea that the early evolution of this wind is nearly adiabatic. The adiabatic phase of the wind evolution is described by the equation for the conservation of energy  $E$  (Ostriker & McKee 1988):

$$\frac{dE}{dt} = \frac{1}{2} \dot{M}_w v_w^2 + \varepsilon 4\pi R^2 \cdot \left\{ \left[ \frac{1}{2} \rho_o v_o^2 + u_o - \rho_o \frac{GM_h}{R} \right] (v_s - v_o) - v_o P_o \right\}, \quad (1)$$

where  $R$  and  $v_s$  are the radius and the velocity of the shock,  $\dot{M}_w$  and  $v_w$  the mass outflow rate and the outflow velocity of the wind,  $\rho_o$ ,  $P_o$  and  $v_o$  the density, the pressure and the outward velocity of the surrounding medium and  $M_h$  the total mass internal to the shock radius. The entrainment fraction parameter  $\varepsilon$  defines the fraction of mass that the wind sweeps up while crossing the ambient medium. Here, we call “entrained” gas the ambient gas which has mixed into the hot bubble phase either through turbulent mixing of shocked diffuse ambient gas or by evaporation and ablation of the filament gas, most of which  $(1 - \varepsilon)$  continues falling onto the galaxy. The latter process is similar to the loading of ISM mass onto stellar winds and supernova blastwaves.

The adiabatic phase is terminated when the loss of energy by radiation becomes substantial and most of the energy transferred to the swept-up gas is radiated away. When the cooling time of the hot bubble becomes shorter than the age of the wind, a thin shell of cooled gas forms near the bubble’s outer boundary and continues to expand pushed by the momentum of the wind. The snowplough phase is described by the equation for the conservation of momentum:

$$\frac{d}{dt} (mv_s) = \dot{M}_w (v_w - v_s) - \frac{GM_h}{R^2} m - \varepsilon 4\pi R^2 [P_o + \rho_o v_o (v_s - v_o)], \quad (2)$$

where  $m$  is the mass of the shell.

In our simulations both bursts of star formation and quiescent star formation can power winds, since we do not explicitly restrict the star formation rate required for a galaxy to blow a wind. It is not possible to predict *a priori* when a wind will escape the gravitational pull of a galaxy, since its evolution and its final fate are linked to several factors, like the star formation and the mass accretion history of the galaxy, the potential well of the dark matter halo in which it expands, the amount of mass accreted from the wind and from the IGM and so on.

In general, a wind receives energy from the starburst and is slowed down by the gravitational attraction of the central galaxy and by the ram pressure of the ambient medium. Thermal pressure effects are included consistently inside cluster haloes, but are neglected in the IGM. If the entrained mass is small (e.g.  $\varepsilon \leq 0.1$ ), a large fraction of

the bubble or shell mass consists of supernova ejecta and shocked ISM, which flow out from the galaxy with a velocity often much larger than the escape velocity of the halo. Since little energy or momentum has to be spent by the wind to accelerate the entrained mass, the shock velocity is less sensitive to energy losses by pressure and gravity. Such a wind is thus more likely to break free from the halo than more mass-loaded winds. When mass-loading is substantial (e.g.  $\varepsilon = 0.3$ ), a significant part of the wind energy is consumed to accelerate the entrained gas and the expansion slows down considerably. If the amount of swept-up mass is large compared to the mass initially ejected, the shock velocity may drop below the escape velocity from the galaxy and the wind collapses back onto the galaxy.

At high redshift winds tend to be mostly momentum-driven, while at lower redshifts bubbles are much more likely to remain adiabatic. This is partly due to the higher mean density of the Universe at high  $z$  and partly to a lower energy input from star formation, which results in lower bubble temperatures and shorter cooling times immediately after blowout. The transition from pressure-driven bubbles to momentum-driven shells may be a first hint that a wind is not powerful enough to escape the galaxy’s attraction. In fact, pressure-driven winds are overall more likely to escape galaxies than momentum-driven ones.

### 3 SIMULATING THE Ly $\alpha$ FOREST

In this section we show how we extract sets of artificial spectra from our simulated region. Since we use a semi-analytic model associated to N-body simulations, we do not have *a priori* all the information about the gas properties provided by a gas-dynamical simulation. We therefore need to estimate quantities like the gas temperature and density, which are necessary to build the spectra, by applying approximate prescriptions. We show how in Subsection 3.1. In Subsection 3.2 we describe how we include the effects of winds in the calculation of the spectra.

We extract lines-of-sight (LOS, hereafter) from our simulated region following the numerical scheme of Theuns et al. (1998). We describe our assumptions about the ionisation state of the gas along the LOS in Appendix A. In Appendix B we summarize our prescriptions for the integration of the relevant quantities along the LOS and for the calculation of the optical depth and the flux spectrum. All spectra are normalized to the mean observed flux of Kim et al. (2004). Gaussian noise is added to the simulated spectra assuming a fixed signal-to-noise ratio of 50, typical of HIRES spectra. Gaussian read-out noise with variance  $0.004^2$  is also added to each pixel.

We extract synthetic spectra from three different sets of simulations: 1) a “no wind” model, in which we do not include the effects of galactic winds; 2) a wind model with low mass loading efficiency and entrainment fraction parameter  $\varepsilon = 0.1$  (hereafter “e01”); 3) a wind model with high mass loading efficiency and entrainment fraction parameter  $\varepsilon = 0.3$  (hereafter “e03”). For each set of simulations we extract spectra at  $z \sim 3$  and  $z \sim 2$ .

For each wind model, we then extract two sets of spectra from our simulated region: i) one set along random directions and ii) one set imposing that the LOS intercept specially se-

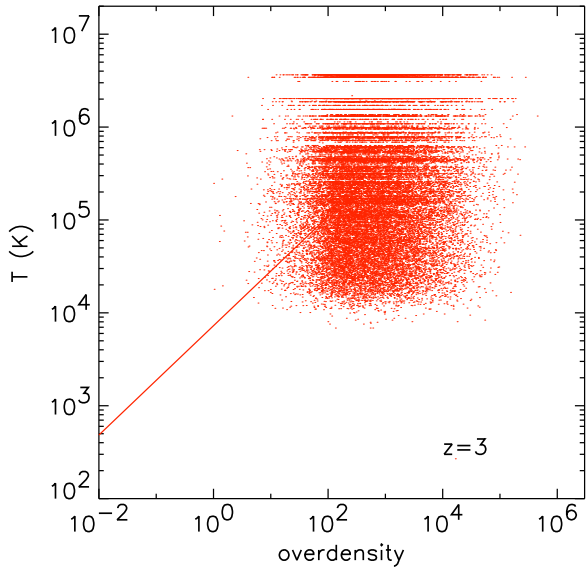


**Figure 1.** The temperature of the gas in M3 at  $z = 3$ . Gas that obeys the equation of state in eq. 4 piles up on the straight line, while the shocked gas in haloes is spread out in a cloud-like region.

lected galaxies at random distances in the interval  $(0, 10) h^{-1}$  Mpc comoving. We use the first sample of spectra to calculate the flux probability distribution function (PDF) and the power spectrum  $P(k)$  and the second to investigate the effects of winds on the surroundings of galaxies. The second set of spectra was selected to match the observations of A05 as accurately as possible. In table 3 of A05 are listed the properties of the galaxies observed by NIRSPEC with impact parameters (e.g. distance galaxy-LOS) smaller than  $1 h^{-1}$  Mpc comoving. According to these data, we select galaxies in our simulation which have: 1) stellar masses larger than  $10^9 M_{\odot}$ ; 2) SFR larger than  $1 M_{\odot}/\text{yr}$ : these two values are the minimum stellar mass and the minimum SFR estimated by A05. In total we extract a sample of about 4400 LOS at  $z \sim 3$  and about 3300 LOS at  $z \sim 2$ : one LOS for every galaxy with the desired properties. We make no requirements about the presence of winds, but we do require that both the selected galaxy and the LOS fall inside our high resolution region.

The set of random spectra has been selected assuming that each LOS passes at a distance of less than half the radius of the high resolution region from the centre of mass of the simulation  $\mathbf{x}_c$ , that is  $d(\text{LOS}, \mathbf{x}_c) < 13 h^{-1}$  Mpc. This is because we want to extract simulated spectra of minimum length  $45 h^{-1}$  Mpc comoving.

### 3.1 Density and temperature of the gas

The gas density in our simulated region is assumed to follow the dark matter density distribution. This is not a very satisfactory description for large matter overdensities, like galaxies or galaxy groups, but it is sufficiently accurate for the gas in low density regions, which represents about 70% of the mass at  $z \sim 3$  and which is responsible for most of

the Ly $\alpha$  forest. The density of the dark matter  $\rho_{\text{DM}}$  is calculated by SPH interpolation and the density of the gas  $\rho_{\text{gas}}$  is recovered by assuming that  $\rho_{\text{gas}} = f_{\text{baryon}} \cdot \rho_{\text{DM}}$ , with  $f_{\text{baryon}}$  the global baryon fraction.

The temperature of the “gas” particles is calculated separately for high density particles bound to haloes and low density unbound particles. This double treatment is necessary since the physical conditions of the gas in the two cases are different. The intergalactic gas is mostly unshocked, cools adiabatically and is photoionised by the UV background radiation. On the other hand, the gas in haloes is shock-heated because of the structure formation process and its temperature is determined by the gravitational potential of the dark matter halo in which it resides. We therefore divide our particles in two subgroups, the “halo” particles and the “IGM” particles, and calculate their temperatures according to different prescriptions.

For “halo” particles we mean all those particles which belong to bound structures and we assume that the temperature of these particles equals the virial temperature of the halo (White & Frenk 1991):

$$T_{\text{vir}} = \frac{\mu m_{\text{p}} V_{\text{c}}^2}{2k_{\text{B}}} = 35.9 \left[ \frac{V_{\text{c}}}{\text{km s}^{-1}} \right]^2 \text{ K}, \quad (3)$$

where  $V_{\text{c}}$  is the circular velocity of the halo,  $\mu$  is the mean molecular weight of the gas,  $m_{\text{p}}$  is the proton mass,  $\mu m_{\text{p}}$  the mean particle mass and  $k_{\text{B}}$  the Boltzmann constant.

The low density “IGM” particles represent the diffuse intergalactic medium and usually have overdensities  $\delta \lesssim 10 - 100$ . For these particles, we calculate the temperature from the equation of state of Hui & Gnedin (1997), which approximates a power law:

$$T = T_{\text{o}} (1 + \delta)^{\gamma - 1}, \quad (4)$$

where  $\gamma - 1 \sim 1/1.7$ .  $T_{\text{o}}$  is the temperature of the IGM at the mean density and can be recovered under the assumption that the gas is in photoionisation equilibrium (Hui & Gnedin 1997, Schaye et al. 2000). In this work, we use the results of Bolton et al. (2004) to define  $T_{\text{o}}$  as a function of redshift.

In figure 1 we show the temperature of the gas in M3 at  $z = 3$ . The low density gas obeying the equation of state (4) is distributed along a straight line, while the high temperature gas in haloes is spread into a cloud-like region. The horizontal lines crossing the cloud are due to gas with different densities residing in the same halo, which is assumed to behave as an isothermal gas sphere. Our prescriptions for the gas temperature are unable to reproduce the cold neutral gas in galaxies and galaxy haloes. This will partly affect our results and we will show how in the following Sections.

### 3.2 The matter displaced by winds

To include the effects of winds in the calculation of a spectrum, we proceed in the following way. As seen in Section 2.2, winds can be described as bubbles of hot gas or as thin shells of cold material accumulating at the edge of a cooled cavity. These two phases of the wind evolution produce different conditions for the material displaced by winds and a separate treatment of bubbles and shells is therefore needed.

Since winds modify the spatial distribution of the gas near galaxies, we need to identify how much mass is displaced, which particles can be associated with the displaced

matter and where this matter moves. All the particles residing outside winds remain unaffected. To do this, we identify all the gas particles positioned inside winds. We then calculate the total amount of mass  $M_{\text{in}}$  inside winds as predicted by the semi-analytic model: this is equal to the sum of the stellar and cold gas mass of galaxies plus the halo or IGM mass inside the wind radius. The total mass contained in bubbles, shells and cavities is  $M_{\text{out}} = \sum (M_w + m_e)$ , with  $M_w$  the mass of the wind ejecta and  $m_e$  the swept-up mass in each wind. We finally define  $F = M_{\text{out}}/M_{\text{in}}$  as the fraction of the baryonic mass in the wind-affected region that belongs to bubbles and shells.

Once  $F$  is calculated, we determine which individual particles are “wind” particles and which ones are not; “wind” particles are ignored when integrating quantities along the LOS and alternative prescriptions are used to calculate the optical depth contributed by winds, as we will show in the following. Since there is no exact or unique way to identify the “wind” particles, we decided to flag as “wind” a fraction  $F$  of all particles in the wind-affected regions, specifically those with the lowest estimated densities. This approximation implies that the particles we remove from the list are generally residing far from the centre of haloes, while the particles representing the galaxy and the unperturbed ambient medium tend to cluster towards the centres. However, since particles have a finite volume, defined by their SPH smoothing radius  $h_i$ , the lowest density particles are also the ones spread over the largest volumes, and so most likely to contribute to the LOS. Contributions from matter “in” galaxies is mostly unaffected.

In our calculations, we first determine the density and the density-weighted temperature and velocity contributed by non-wind particles to each bin  $j$  along a LOS (Appendix B). We then add in the contribution of the winds themselves. Finally, we calculate the optical depth along the LOS and the flux spectrum. In Subsections 3.2.1 and 3.2.2 we show how we estimate the contributions of bubbles and shells respectively and we discuss a few examples of synthetic spectra.

### 3.2.1 Contribution by bubbles

To calculate the contribution of bubbles to the optical depth along a LOS, we assume that the material outflowing from the galaxies and the shocked ambient medium are efficiently mixed and uniformly distributed inside the bubble. This assumption of a uniform bubble is reasonable (although not exact), because the sound crossing time of the gas is shorter than the dynamical time of the wind.

The semi-analytic description of the wind evolution gives information about the mass, radius, velocity and temperature of the wind. The temperature of the bubble  $T_b$  is determined by the energy balance in the wind (cfr. eq. 4 of BSW05). Most temperatures are of order  $10^5$  to few times  $10^6$  K, which means that the bubble material is collisionally ionised. We calculate the fraction of neutral hydrogen  $X_{\text{H I}}$  in a bubble by assuming collisional ionisation equilibrium (Appendix A).

The neutral hydrogen density and the density-weighted temperature and velocity that a bubble contributes to each

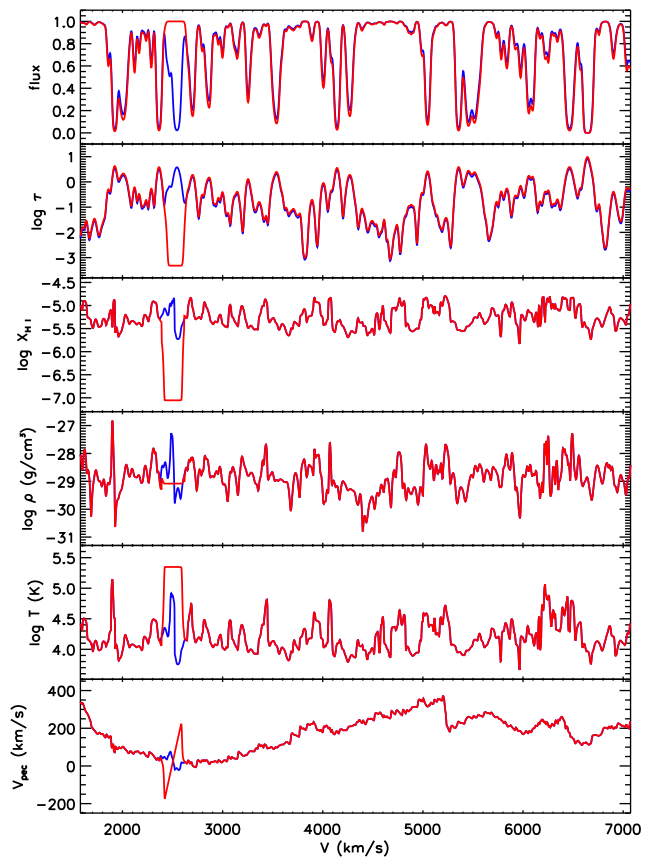


**Figure 2.** Example of spectrum crossing a pressure-driven bubble. The blue line shows the unperturbed “no wind” model, the red line the e03 wind model. From top to bottom, the different panels reproduce the flux spectrum, the optical depth  $\tau$  of the gas along the line of sight, the fraction of neutral hydrogen  $X_{\text{H I}}$ , the total density  $\rho$ , the temperature  $T$  and the peculiar velocity  $v_{\text{pec}}$ .

bin  $j$  which intercepts the bubble, are:

$$\rho_{\text{H I}}(j) = a^3 X_{\text{H I}} \rho_b, \quad (5)$$

$$(\rho T)_{\text{H I}}(j) = a^3 X_{\text{H I}} \rho_b T_b, \quad (6)$$

$$(\rho v)_{\text{H I}}(j) = a^3 X_{\text{H I}} \rho_b v_{\text{pec,b}}, \quad (7)$$

where  $a$  is the scale factor,  $\rho_b$  the bubble density and  $v_{\text{pec}}$  the projection of the peculiar velocity of the wind on the LOS.

In Fig. 2 we show an example of the build-up of a spectrum along a LOS that crosses a bubble. From top to bottom, the panels show the flux spectrum, the optical depth  $\tau$ , the fraction of neutral hydrogen  $X_{\text{H I}}$ , the total density  $\rho$ , the temperature  $T$  and the peculiar velocity  $v_{\text{pec}}$  of the gas along the LOS. The blue line represents the unperturbed quantities calculated from the “no wind” model, while the red line is for the perturbed quantities from the e03 model. In this spectrum, the LOS intersects a large bubble at a small distance from the source galaxy, but does not intercept the galaxy itself. The ionised gas inside the bubble produces a decrease of the optical depth, due to its high temperature

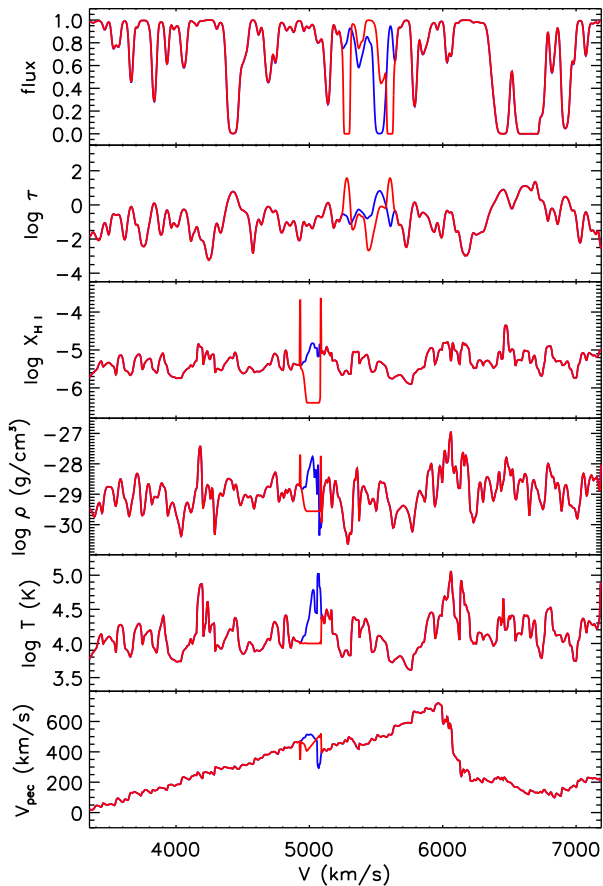


**Figure 3.** Example of spectrum crossing a momentum-driven shell. The quantities shown are the same as for Fig. 2 for the unperturbed “no wind” model (blue line) and for the e03 wind model (red line).

and ionisation state. The “Z” shape in the velocity distribution of the gas along the LOS (bottom panel) is due to the outflowing wind material,  $v_s \sim 200 \text{ km s}^{-1}$ , which modifies the velocity field around the galaxy.

The flux spectra and the optical depth differ slightly in the two cases because of normalization effects: this happens when winds modify the mean optical depth along the LOS by more than a few percent and an iteration or two is needed during the normalization process. However, the final difference between the “wind” and the “no wind” models after normalization is always less than a few percent, even in the most extreme cases.

### 3.2.2 Contribution by shells and cavities

The effect of shells on the opacity of the gas along a LOS is substantially different from that of bubbles. Both the shell and the cavity evacuated in its interior are cold, and have a more complex density structure. When winds cool down, part of the outflowing wind mass and all the swept-up mass accumulate in a thin shell. A cavity is left behind, in which the low-density, cooled wind material that has not yet reached the shell flows outwards at the wind velocity. The mass that accumulates in the shell occupies a small

volume and its density can become significantly higher than the density of the surrounding medium.

We make the assumption that the temperature of shells and cavities is constant and equal to  $T_s = 10^4 \text{ K}$ . This assumption is motivated by the fact that, after the wind cools down and all the energy is radiated away, the outflowing material reaches photoionisation equilibrium with the UV background and will maintain this temperature as long as the density of the shell is not too high.

Our semi-analytic model does not give an explicit description of the density structure of shells and cavities, but we can reconstruct it by solving the appropriate set of shock conditions. We use the Rankine–Hugoniot jump conditions for a non-relativistic shock to calculate the pressure  $P_s$  of the gas in the shell. If we assume that the velocity of the gas behind the shock is equal to the shock velocity  $v_s$ , we obtain:

$$P_s = P_{\text{igm}} + \rho_{\text{igm}} (v_s - v_{\text{igm}})^2, \quad (8)$$

where  $\rho_{\text{igm}}$ ,  $v_{\text{igm}}$  and  $P_{\text{igm}}$  are the density, the velocity and the pressure (thermal plus ram) of the ambient medium. The density of the shell  $\rho_s$  is then given by the equation of state:

$$\rho_s = \frac{\mu m_p P_s}{k_B T_s}. \quad (9)$$

The radius  $R_c$  of the cavity internal to the shell is given by:

$$R_c^3 = R^3 - \frac{3m}{4\pi\rho_s} \quad (10)$$

and the thickness of the shell is  $R_s = R - R_c$ , with  $m$  the shell mass. The density of the cavity is determined by the wind mass which has not yet reached the shell  $M_c$  and is given by  $\rho_c = 3M_c/4\pi R_c^3$ .

We estimate the contribution of shells and cavities to the neutral hydrogen density and the density-weighted temperature and velocity along the LOS by using eqs. (5), (6) and (7), where the index “ $b$ ” has been changed with “ $c$ ” and “ $s$ ”. Shells affect only a few bins on the outer edge of a wind penetrated by a LOS. The number of the bins is determined by the thickness of the shell, which is normally as large as the linear dimension of few bins (typically, the bin width is about  $20\text{--}26 h^{-1} \text{ kpc}$ ). The remaining bins inside the shell get contributions from the cavity gas.

In Fig. 3 we give an example of the build-up of a spectrum that crosses a shell. The quantities shown are the same as in Fig. 2. The shell crossed by the LOS has a density about ten times the density of the ambient medium, but the fraction of  $\text{H I}$  in the shell is about 100 times higher. The cold neutral gas in the shell produces two almost symmetric spikes in the optical depth, which appear as two narrow and saturated absorption lines in the flux spectrum. The temperature of  $10^4 \text{ K}$  that we assume for the shell determines the small width of the lines, while the high neutral fraction produces the saturation.

The LOS in Fig. 2 and 3 show examples of the effects of winds in spectra. In general, a line of sight may not cross any wind at all or it may cross several, in which case the spectrum may become more confused.

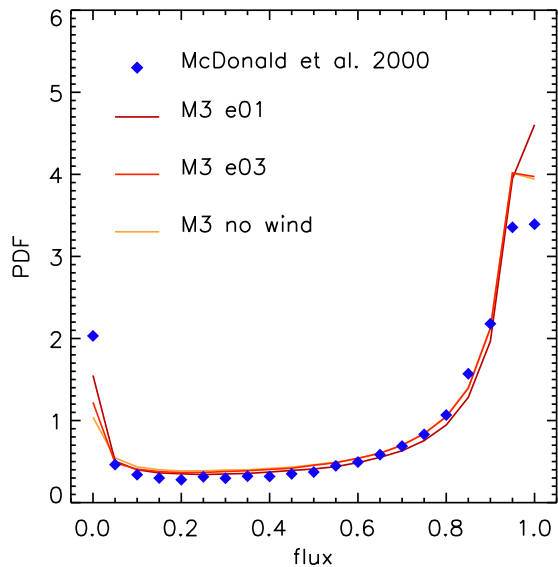


**Figure 4.** Flux PDF for the Ly $\alpha$  forest at  $z = 3$ . The numerical results are compared to the observations of McDonald et al. (2000).

#### 4 FLUX PDF

We calculate the flux probability distribution function (PDF) as a first comparison between our simulated spectra and the observations. We use about 600 spectra from our random sample at  $z = 3$  and we compare the results with the observations of McDonald et al. (2000). Fig. 4 shows our results for the “no wind” model and for the e01 and e03 wind models. The agreement between the observations and our three sets of simulations is in general very good and deviations from the observed values are significant only at fluxes  $F \sim 0$  and  $F > 0.9$ .

In general, the e03 model gives almost exactly the same result as the “no wind” model, while a small but more significant difference is evident with the e01 model. This may be an indication that the weak winds predicted by the e03 model are unable to affect the flux PDF of the Ly $\alpha$  forest, while more efficient winds as in the e01 model may slightly modify it. However, in all cases the difference between the numerical results and the observations are tiny, and not sufficient to rule out any of the feedback models.

#### 5 POWER SPECTRUM

To calculate the power spectrum of the flux, we use the estimator proposed by Hui et al. (2001). Since the power spectrum is sensitive to changes in the mean spectral flux  $\langle e^{-\tau} \rangle$ , which is a function of redshift, Hui et al. (2001) suggest calculating the power spectrum of the quantity:

$$F = \frac{e^{-\tau}}{\langle e^{-\tau} \rangle} - 1, \quad (11)$$

where  $\tau$  is the optical depth and  $e^{-\tau}$  the amplitude of the fluctuations. Fig. 5 shows our results for the power spectrum of the transmitted flux  $P(k)$ , calculated in this way from

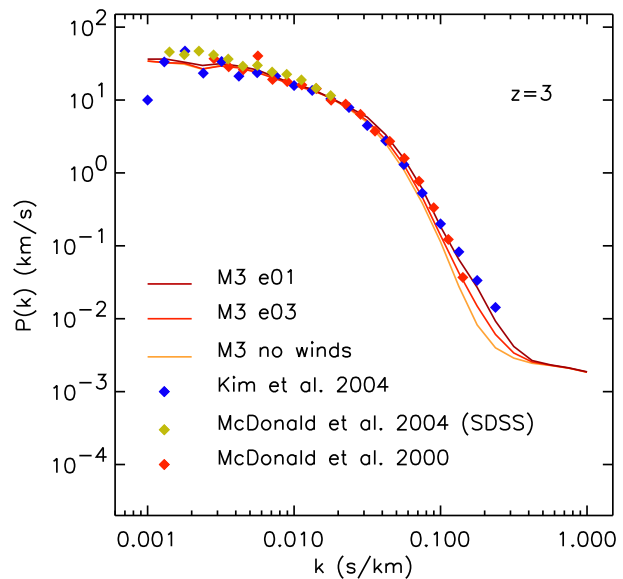


**Figure 5.** The flux power spectrum computed from synthetic spectra at  $z \sim 3$ . The numerical results are compared to the observations of Kim et al. (2004) at  $z \sim 2.54$ , McDonald et al. (2000) at  $z = 3$  and McDonald et al. (2004) at  $z = 3$ . The synthetic spectra have been calculated using the samples of randomly selected LOS for the “no wind”, e01 and e03 models.

the sets of random spectra at  $z = 3$  for the “no wind”, e01 and e03 models. The numerical results are compared to the observations of Kim et al. (2004), McDonald et al. (2000) and McDonald et al. (2004). Kim et al. (2004) and McDonald et al. (2000) compute the power spectrum from few high resolution quasar spectra taken with the VLT and Keck telescopes respectively, while McDonald et al. (2004) use a sample of about 3000 medium resolution spectra from the Sloan Digital Sky Survey (SDSS). The lower resolution of the SDSS spectra limits the estimate of  $P(k)$  in the range  $0.0013 - 0.04 \text{ s km}^{-1}$ , while higher resolution spectra allow to estimate  $P(k)$  in the broader range  $0.001 - 0.2 \text{ s km}^{-1}$ . At  $k > 0.3 - 0.4 \text{ s km}^{-1}$   $P(k)$  is dominated by noise and flattens out.

In Fig. 5 there is agreement between the “no wind” model and the e01 and e03 wind models at  $k < 0.1 \text{ s km}^{-1}$ , with deviations appearing only at smaller scales. At  $k \gtrsim 0.1 \text{ s km}^{-1}$  the three numerical models diverge and, broadly speaking, the higher the wind efficiency, the more power is contributed at smaller scales. This is consistent with our previous results for the wind filling factor and the fraction of IGM mass in winds (BSW05), which predict that, although winds may not heavily modify the statistical properties of the Ly $\alpha$  forest, the largest deviations should be found in the e01 model. In addition, the fact that more efficient winds contribute more power on small scales is consistent with the presence of the narrow and saturated absorption lines created by shells, which are more numerous in the e01 model. These lines contribute power to scales smaller than about a hundred kiloparsecs.

Unfortunately, the spectral region corresponding to  $k \gtrsim 0.1 \text{ s km}^{-1}$  is also the region where unidentified metal lines (principally O VI) blended with the Ly $\alpha$  forest might give

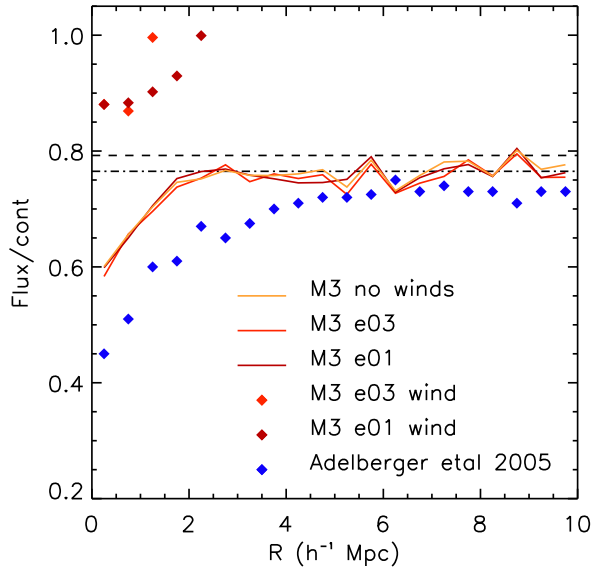


**Figure 6.** The mean flux transmissivity around LBG as a function of the impact parameter. Results are presented for a sample of about 7700 simulated galaxies with random impact parameters (lines) and for subsamples of galaxies blowing winds with radii larger than the impact parameter (diamonds). The observational data are from A05.

a substantial contribution to the power. Although we are tempted to suggest that both our wind models seem to fit the data better than the “no wind” model, we cannot definitely rule out the “no wind” model itself, since our current Ly $\alpha$  spectra do not include metal lines and we are unable to estimate well how much power is contributed by them.

The good agreement between the two wind models and the “no wind” model at  $k < 0.1 \text{ s km}^{-1}$  is an indication that the effects of galaxy feedback on the Ly $\alpha$  forest, and in particular of galactic winds, should not affect the estimation of cosmological parameters.

## 6 FLUX TRANSMISSIVITY AROUND LBG

In this Section we present our results for the mean Ly $\alpha$  flux transmissivity near Lyman break galaxies and we investigate the effect of winds on the absorption spectra at small impact parameter. We use our sample of galaxy-selected spectra at  $z = 3$  and  $z = 2$  for the “no wind”, e01 and e03 models (Section 3).

Fig. 6 shows our results for the mean transmitted flux as a function of the impact parameter  $R$ . The numerical results are compared to the observations of A05. The analysis of our full set of spectra confirms the observation that the mean Ly $\alpha$  transmissivity near LBGs decreases for small impact parameters. Our spectra yield a smaller decrease than seen in the observations: this is partly due to the fact that our semi-analytic prescriptions are unable to describe the cold neutral gas in haloes and simply assume that this gas is at the virial temperature and so highly ionised. In addition, the mean flux  $\langle F \rangle = 0.792$  in the simulated spectra is higher than in the data, where  $\langle F \rangle = 0.765$ . This is not a severe

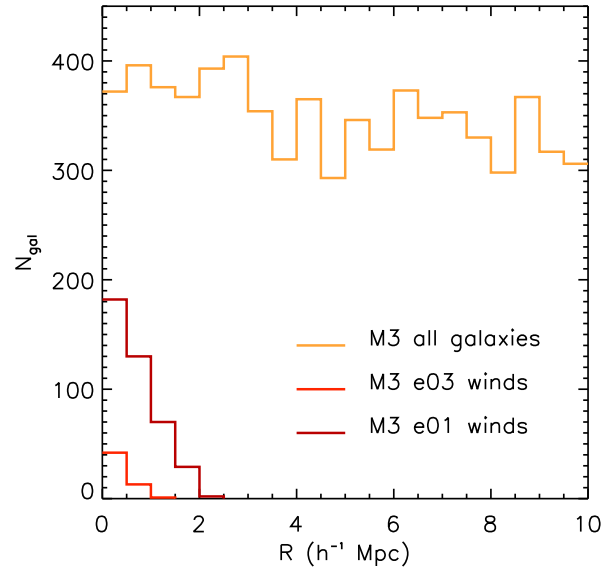


**Figure 7.** The total number of galaxies and the number of wind-blown galaxies with wind radii larger than the impact parameter as a function of impact parameter in the simulated sample.

problem, however, because the difference is small and all our models do predict a non-negligible decrease in the Ly $\alpha$  flux.

A more detailed analysis shows that the Ly $\alpha$  flux is almost completely transmitted around a significant fraction of the galaxies in our model and that the gas in these regions has an extremely low optical depth. This is shown in Fig. 6 by the diamonds in the upper left corner, which represent the mean transmitted flux along those LOS that actually intercept wind bubbles. These galaxies show transmitted fluxes up to 50–60% higher than the mean flux found for the full sample.

In Fig. 7 we show the total number of LOS and the number of intercepted wind bubbles in the e01 and e03 models as a function of impact parameter. Since we assign random impact parameters when extracting the LOS, the distribution of the total number of galaxies is close to uniform. The e01 model produces wind-blown galaxies with bubble radii as large as  $2.5 h^{-1} \text{ Mpc}$ , while fewer winds and maximum radii of  $1.5 h^{-1} \text{ Mpc}$  are produced by the e03 model. The fraction of galaxies for which the LOS intercepts a bubble for impact parameters below  $1 h^{-1} \text{ Mpc}$  is about 7% for the e03 model and about 40% for the e01 model. These numbers are in good agreement with the finding of A05 that about a third of the galaxies in their sample show almost complete transmission of the quasar Ly $\alpha$  flux at the LBG redshift.

Winds either evacuate cavities or drive bubbles of hot gas into their surroundings. Although the physics of pressure-driven and momentum-driven winds is different, in either case the optical depth of the gas may be reduced inside the wind, and the flux increased. In the case of adiabatic winds, the hot gas in bubbles is highly ionised, bubble temperatures being normally higher than  $10^5 \text{ K}$ . In case of momentum-driven winds, the swept-up gas accumulates into a thin shell, while a cavity is evacuated in the interior, where only the cooled wind is flowing outwards. The density

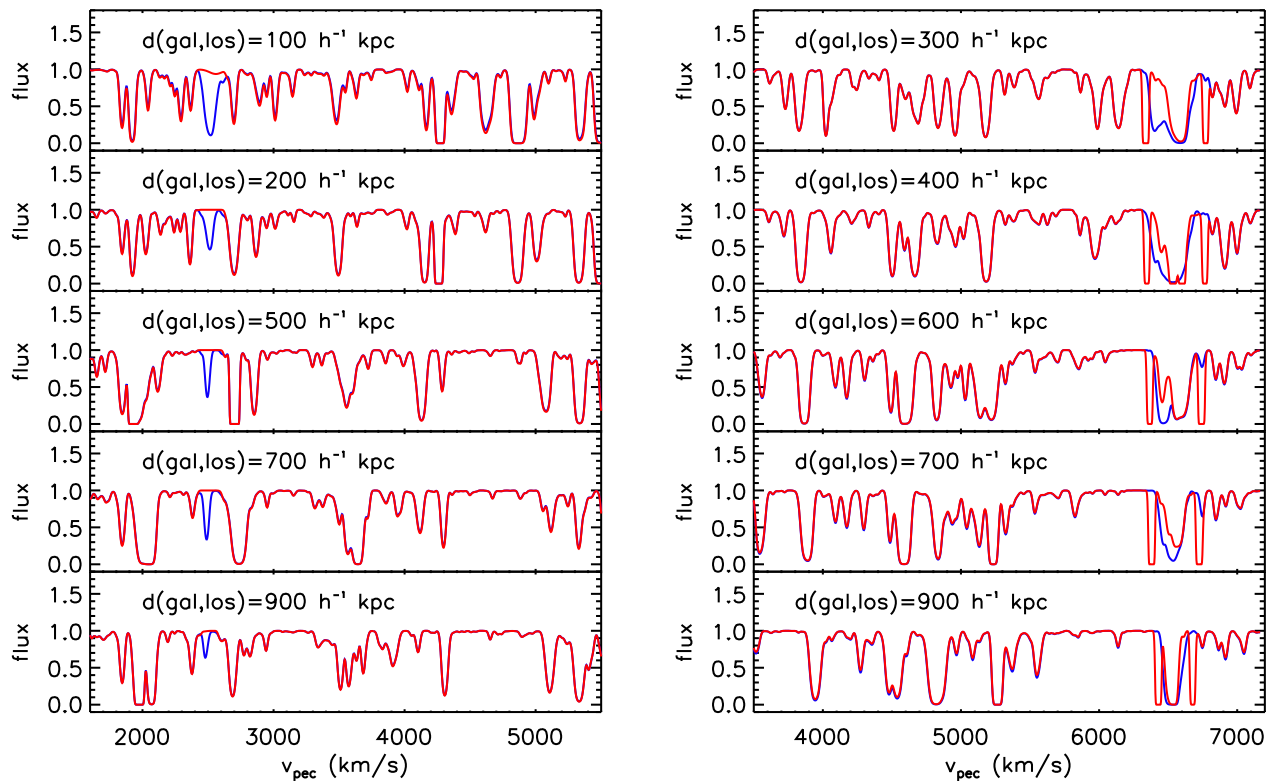


**Figure 8.** Two sets of parallel lines of sight intercepting isolated field galaxies blowing winds into the IGM at impact parameters  $100 < b < 900 h^{-1}$  comoving kpc. The left panel shows how the absorption from neutral gas surrounding a galaxy is quenched inside a hot pressure-driven bubble. The right panel shows the effect of a momentum-driven wind and the absorption by the cold gas in the shell. The red line represents the spectrum perturbed by winds from the e03 model, while the blue line the unperturbed spectrum from the “no wind” model. The galaxy in the left panel has  $M_* = 1.6 \cdot 10^9 h^{-1} M_\odot$  and is blowing a bubble with radius  $R = 257 h^{-1}$  (physical) kpc, velocity  $274 \text{ km s}^{-1}$  and temperature  $T = 2.2 \cdot 10^5 \text{ K}$ . The galaxy in the right panel has  $M_* = 9.2 \cdot 10^9 h^{-1} M_\odot$  and is pushing a shell with radius  $R = 272 h^{-1}$  (physical) kpc and velocity  $103 \text{ km s}^{-1}$ .

of the residual gas inside the cavity is tiny and its contribution to the optical depth along the LOS is generally negligible. Occasionally another absorber external to the galaxy may intervene to produce an uncorrelated absorption line.

In Fig. 8 we show the effects of winds on artificial spectra at various impact parameters from source galaxies in the e03 wind model. For clarity, we have chosen two isolated field galaxies with wind radii larger than  $1 h^{-1}$  comoving Mpc and with no other wind-blowing galaxies in their proximity. In regions where galaxies are more clustered, winds overlap and their signatures in spectra mix and become less easily identifiable. The left panel shows the effect of a pressure-driven bubble of hot gas that ionises the gas surrounding the source galaxy (see also Fig. 2). Since there are no intervening absorbers along the LOS, the bubble increases the flux transmissivity in the spectral region corresponding to the galaxy position. The right panel shows a momentum-driven shell that evacuates a cavity and accumulates material at its edges (see also Fig. 3). The symmetric pattern of two narrow and saturated absorption lines is clearly visible. The separation between the two absorption lines and the pixel corresponding to the minimum distance to the galaxy is roughly equal to the velocity of the shell projected onto the LOS.

In Fig. 9 we show the distribution of galaxies with im-

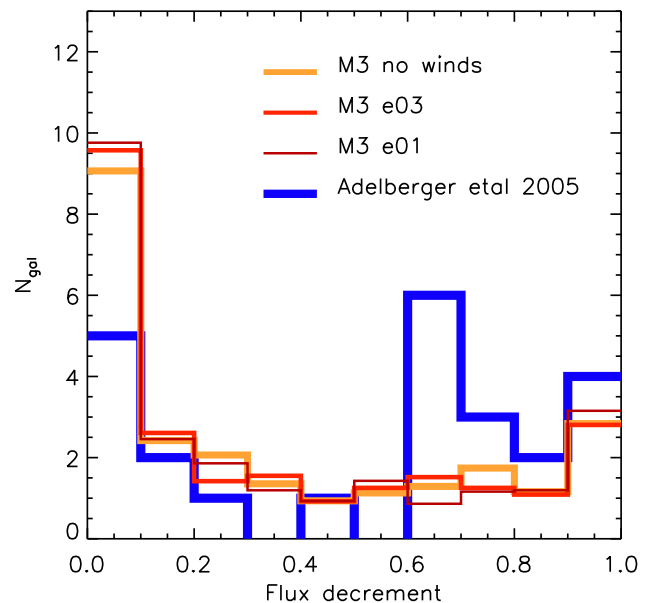


**Figure 9.** The distribution of galaxies with impact parameter  $b < 1 h^{-1} \text{ Mpc}$  as a function of the flux decrement observed in the spectra. The observational data are from A05.

pact parameter smaller than  $1 h^{-1}$  Mpc as a function of the flux decrement. The numerical results are compared with the data of A05 and normalized to the total number of objects in the observational sample (e.g. 24 galaxies). The flux decrement is defined as  $F_D = 1 - F$ .

A05 claim that numerical simulations are unable to reproduce the high number of galaxies with  $F_D \sim 0$  found in their data. In Fig. 9 we show that this is not the case for our model, independent of the wind parameters. In fact, the distribution of galaxies as a function of the flux decrement is an alternative way to represent the PDF of the flux in the spectra and, if the impact parameters of the LOS are randomly chosen in the interval  $(0, 1)h^{-1}$  Mpc, then the distribution of galaxies in Fig. 9 should qualitatively look like the PDF of the flux in Fig. 4, where the  $x$ -axis has been inverted from  $F$  to  $F_D = 1 - F$ . The simulation result presented by A05 that almost no galaxies have  $F_D \sim 0$  could be understood if the impact parameter of the galaxies in the sample is close to 0 or smaller than the virial radius. In this case, a LOS would intercept the reservoir of neutral hydrogen in the halo/disk of the galaxy and a large flux decrement should be expected. Although our galaxy distribution explains the relatively high number of galaxies with  $F_D \sim 0$ , a more detailed comparison between our data and the observations is inconclusive. In fact, the 24 observed galaxies are too few to define a distribution calculated over 10 bins. For comparison, we have almost 800 galaxies in our model sample. The e01 and e03 wind models predict a slightly larger number of galaxies with small flux decrements than the “no wind” model, in agreement with what we showed in Fig. 6.

## 7 GAP STATISTICS

We showed in the previous sections that winds do leave specific signatures in the Ly $\alpha$  forest, although they may not strongly affect the flux PDF and the flux power spectrum. In this section, we present a new method to test statistically for the presence of wind absorption lines in the Ly $\alpha$  forest. The method is based on two findings: first, when a LOS crosses a shell, a narrow and saturated absorption line is created; secondly, these absorption lines due to shells appear to have roughly all the same line width and steep profile. We look for shell absorption lines in our artificial spectra by identifying all the spectral regions where absorption is complete. To select such regions, we require that the flux is smaller than  $F < 0.1$  throughout. We estimate the width in wavelength of each region, which we call  $D_s$ , and finally we calculate the distribution of the saturated regions as a function of the region width  $D_s$ .

Our results are shown in Fig. 10 for  $z = 3$  and  $z = 2$ . The distribution of saturated regions is not affected by winds except for very small values of  $D_s$ , where absorption lines due to shells in the wind models almost double the number of saturated regions with  $0.3 < D_s < 1 \text{ \AA}$  at  $z = 3$ . At  $z = 2$ , where the number and the width of saturated regions shrinks significantly because of the cosmic expansion and the increased intensity of the UV background radiation, the wind models produce almost three times as many lines with  $0.1 < D_s < 0.6 \text{ \AA}$  as the “no wind” model. This analysis cannot be directly translated into a distribution of lines as a function of column density, because the width of saturated

regions  $D_s$  is by no means a direct estimate of the column density of the absorber. However, our results show that the presence of absorption lines due to shells should significantly increase the number of narrow saturated absorption lines.

We then tried a similar analysis to test for the presence of bubbles. In analogy to what we did for shells, we start from the result that bubbles may enhance the transmissivity of the Ly $\alpha$  flux in their interior, sometimes completely washing out the absorption by neutral gas. We therefore look for “gaps” in the Ly $\alpha$  forest and we identify all the regions with fluxes  $F > 0.9$ , calling their width  $D_g$ . We then calculate the cumulative distribution of the gaps as a function of this width. If bubbles had a large effect on the distribution, we would expect to find an increase in the number of gaps at the largest widths. The effect should be stronger at  $z = 3$  than at  $z = 2$ , since the gap width in the absence of bubbles tends to be larger at lower redshift because of the lower mean opacity of the IGM.

As can be seen in Fig. 11, we do find such an effect, which is particularly significant for the e01 model. This model predicts up to 50% more gaps with  $10 < D_g < 20 \text{ \AA}$  and about 5–20% more gaps with  $5 < D_g < 10 \text{ \AA}$  at both redshifts. For  $10 < D_g < 20 \text{ \AA}$  the e03 model shows a maximum deviation of about 20% from the “no wind” model at  $z = 3$  and almost no deviation at  $z = 2$ . At smaller gap widths there is no difference from the “no wind” model. The larger deviations from the “no wind” model in the results for the e01 model can be understood when two main properties of the winds are considered: i) the total number of wind-blowing galaxies is about ten times larger in the e01 model than in the e03 model; ii) the fraction of pressure-driven bubbles in the e01 model is two times larger than in the e03 model. The maximum radius of bubbles in the e01 model is also larger than in the other model.

The effect of bubbles may be difficult to distinguish in real spectra. The unperturbed cumulative distribution of gaps is unknown and no direct comparison is available. Metal lines may somewhat alter the distribution itself, but this problem could in principle be overcome, because only high column density metal lines not blended in the Ly $\alpha$  forest would affect the distribution, and these should be relatively straightforward to identify and remove. Although the first problem is more difficult to address, we believe that the effect of bubbles in spectra could still be successfully investigated. In fact, in Fig. 11 the cumulative distribution of gaps in unperturbed spectra closely follows a power law relation, while wind models introduce a “bump” in the distribution for  $10 < D_g < 20 \text{ \AA}$ . This deviation from a power law, as we mentioned in the previous paragraph, can be as high as 50% for the e01 model and it could be used to test for the presence of winds in spectra: on the basis of our result, if the cumulative distribution follows a power law, most likely there are no bubble signatures in spectra; on the other hand, if a bump does appear in the cumulative distribution at  $10 < D_g < 20 \text{ \AA}$ , then hot winds may leave a detectable footprint in the forest.

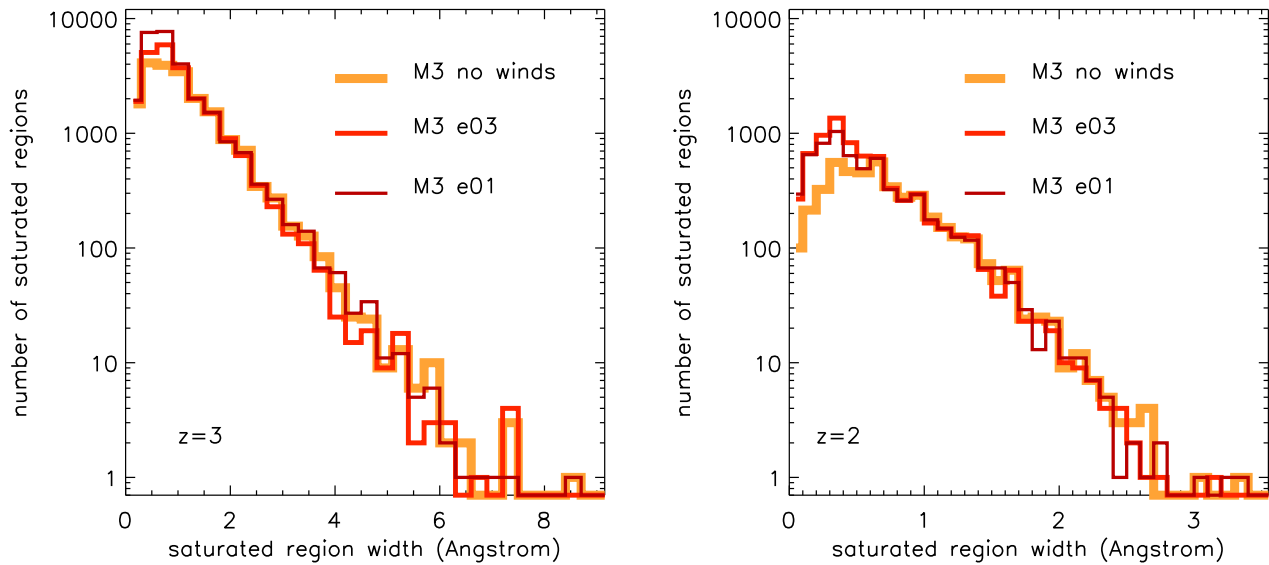


**Figure 10.** The number distribution of saturated regions as a function of region width. Results are shown at  $z = 3$  (left panel) and  $z = 2$  (right panel). Shells contribute a large number of saturated lines with widths smaller than about  $1 \text{ \AA}$ .

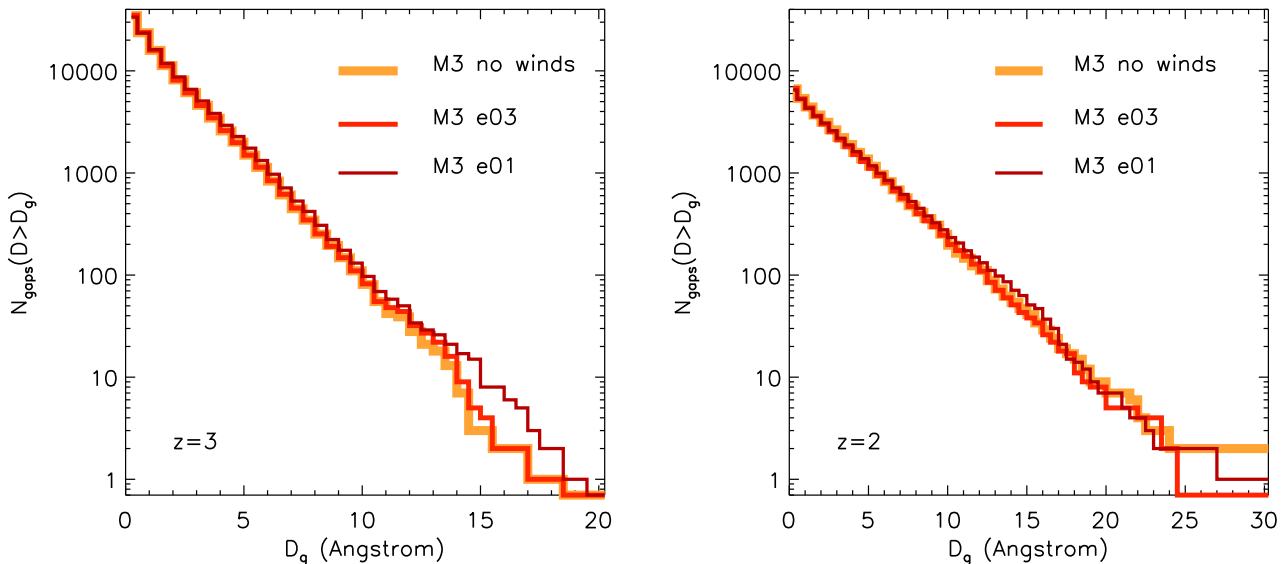


**Figure 11.** The cumulative distribution of gaps in spectra as a function of gap width. Results are shown at  $z = 3$  (left panel) and  $z = 2$  (right panel). The distribution of gaps in the e01 model is mostly affected for gap widths  $10 \lesssim D_g \lesssim 20 \text{ \AA}$  while the e03 model shows a much smaller deviation from the “no wind” model.

## 8 CONCLUSIONS

In this paper, we have used numerical simulations to investigate the effect of galactic winds on the Ly $\alpha$  forest. Our main conclusions can be summarized as follows:

(i) The flux PDF calculated from simulated spectra agrees well with the flux PDF of McDonald et al. (2000) at  $z = 3$  for all three wind models. The effects of the winds are barely discernible the PDF. The small deviations ob-

served between the numerical results and the observational data are insufficient to rule out any of the models.

(ii) Our simulated power spectra of the Ly $\alpha$  flux at  $z = 3$  agree well with the observational results of Kim et al. (2004), McDonald et al. (2000) and McDonald et al. (2004) on all scales, with the e01 wind model closely matching the Kim et al. (2004) data and the e03 model best fitting the data of McDonald et al. (2000) on small scales. The “no wind” model tends to underestimate the power on the smallest scales. Winds sensibly increase the power on scales  $k \gtrsim 0.1$

s km<sup>-1</sup> at  $z = 3$ , when both the volume filling factor  $f_v$  and the fraction of IGM mass in winds  $f_m$  are small. The overall effect is not large, however, and deviations affect only the spectral region which is already contaminated by metal lines. Since  $P(k)$  is not affected by winds on large scales ( $k < 0.1$  s km<sup>-1</sup>), the estimation of cosmological parameters using the Ly $\alpha$  forest flux power spectrum should be insensitive to galactic winds.

(iii) The Ly $\alpha$  flux transmissivity is enhanced near wind-blowing galaxies, independent of whether the wind is creating a bubble of hot gas or a cooled cavity surrounded by a shell. This is consistent with the observations of A05, who find that up to a third of all the galaxies in their sample with impact parameter smaller than  $1h^{-1}$  Mpc have transmitted fluxes up to 90%. The mean Ly $\alpha$  transmissivity decreases with decreasing impact parameter, in agreement with previous numerical models and the A05 data.

(iv) To search for wind signatures in quasar spectra, we have devised a new method which measures the abundance of saturated regions as a function of their width. We find that absorption due to wind shells increases the expected number of saturated regions with  $D_s \lesssim 1 \text{ \AA}$  by a factor of two or more at  $z = 3$  or 2, forcing the distribution to behave as a power law down to smaller widths than in the “no wind” model. In fact, the “no wind” model shows a turn-over at  $D_s \sim 1 \text{ \AA}$  at  $z = 3$  and at  $D_s \sim 0.6 \text{ \AA}$  at  $z = 2$ , while the wind models have such a point at  $D_s \sim 0.5$  and  $D_s \sim 0.2 \text{ \AA}$  respectively. Although not a huge effect, this is certainly large enough to be detectable. Since we consider saturated regions widths rather than line column densities, this measure has the advantage of being insensitive to unsaturated metal lines blended with the Ly $\alpha$  forest.

(v) A similar analysis aimed to estimating the abundance of gaps in the absorption pattern of the Ly $\alpha$  forest shows a weaker but still detectable effect from wind bubbles. We have calculated the cumulative distribution of gaps as a function of the gap width and we find that winds contribute as much as 50% more gaps with  $10 < D_g < 20 \text{ \AA}$  in the e01 model. We suggest that this effect may be used to test the presence of hot winds in the Ly $\alpha$  forest: if the cumulative distribution of gaps closely follows a power law, then it is likely that no winds are present, while if a bump appears for  $10 < D_g < 20 \text{ \AA}$ , then, according to our model, the Ly $\alpha$  forest does contain wind signatures.

(vi) The two new methods we present in Section 7 do not tell us directly *where* wind signatures are, but only *whether* they are present or not. However, this is already a significant improvement with respect to previous works. Finally, the detection of a large bump in the mentioned range may give us an indication that the powerful winds with low entrainment fractions of the e01 model are more likely to occur in the Universe than the weaker and more mass loaded winds in the e03 model.

## ACKNOWLEDGMENTS

This work has been supported by the Research and Training Network “The Physics of the Intergalactic Medium” set up by the European Community under contract HPRN-CT-2000-00126. SB was partially supported by PPARC.

## APPENDIX A: HYDROGEN IONISATION STATE

To calculate how much radiation of a desired wavelength is absorbed by a gas cloud, we need to know the ionisation state of the gas, which determine its optical depth. To calculate the fraction of neutral hydrogen  $X_{\text{H I}}$  in a gas, we solve the equation for ionisation evolution of hydrogen. In the limit of ionisation equilibrium and for a highly ionised gas, we find (Cen 1992, Theuns et al. 1998):

$$X_{\text{H I}} = \frac{\alpha_{\text{H II}} n_e}{\Gamma_{\gamma \text{H I}} + \Gamma_{\text{eH I}} n_e}, \quad (\text{A1})$$

where  $n_e$  is the electron number density,  $\alpha_{\text{H II}}$  the recombination rate of hydrogen,  $\Gamma_{\gamma \text{H I}}$  the photoionisation rate of hydrogen and  $\Gamma_{\text{eH I}}$  the collisional ionisation rate. The recombination rate of hydrogen is a function of the temperature of the gas and, defining  $T_n = T/(10^n \text{ K})$ , is given by (Haardt & Madau 1996):

$$\alpha_{\text{H II}} = \begin{cases} 1.58 \cdot 10^{-13} T_4^{-0.51}, & T \leq 10^4 \text{ K} \\ 1.58 \cdot 10^{-13} T_4^{-0.51-0.1 \log T_4}, & T > 10^4 \text{ K} \end{cases} \quad (\text{A2})$$

Hydrogen is ionised through two different mechanisms: collisional ionisation and photoionisation. Photoionisation is the dominant process in the low density gas with  $T \lesssim 10^5$  K. The photoionisation rate depends on the flux spectrum of the ionising UV background radiation  $J(\nu, z)$ :

$$\Gamma_{\gamma \text{H I}}(z) = \int_{\nu_{\text{H}}}^{\infty} \frac{4\pi J(\nu, z) \sigma_{\text{H}}(\nu)}{h\nu} d\nu, \quad (\text{A3})$$

where  $\sigma_{\text{H}}(\nu)$  is the photoionisation cross-section and  $\nu_{\text{H}}$  the ionising threshold frequency of hydrogen. We use the ionising UV background  $J(\nu, z)$  and the photoionisation rate  $\Gamma_{\gamma \text{H I}}(z)$  of Haardt, Madau & Rees (1999). At temperatures higher than about  $10^5$  K, ionisation by collisional excitation becomes the dominant mechanism. In this regime, the collisional ionisation rate is (Cen 1992, Theuns et al. 1998):

$$\Gamma_{\text{eH I}} = 1.17 \times 10^{-10} T^{0.5} e^{-157809.1/T} \frac{1}{1 + T_5^{0.5}} \text{ cm}^3 \text{ s}^{-1}. \quad (\text{A4})$$

## APPENDIX B: OPTICAL DEPTH AND FLUX SPECTRUM

The optical depth of the gas is calculated by integrating the relevant quantities (density, temperature and velocity) along a given LOS. We identify a sightline through the high resolution sphere and we divide its total length  $L$  into  $N$  pixels of equal width  $\Delta = L/N$ . We choose  $N = 3000$ . The density and the density-weighted temperature and velocity for each bin  $j$  at position  $x(j)$  are computed by integrating the relevant quantities along the LOS (Theuns et al. 1998):

$$\rho_{\text{X}}(j) = a^3 \sum_i X(i) \mathcal{W}_{ij}, \quad (\text{B1})$$

$$(\rho T)_{\text{X}}(j) = a^3 \sum_i X(i) \mathcal{W}_{ij} T(i), \quad (\text{B2})$$

$$(\rho v)_{\text{X}}(j) = a^3 \sum_i X(i) \mathcal{W}_{ij} \{a \dot{x}(i) + \dot{a} [x(i) - x(j)]\}, \quad (\text{B3})$$

where the sum is over all the particles intersecting the LOS.  $a$  is the scale factor and  $X(i)$  is the abundance of the species  $X$  for particle  $i$ , assuming ionisation equilibrium. For Ly $\alpha$  absorption spectra,  $X$  is the neutral hydrogen H I. The normalised SPH kernel is:

$$\mathcal{W}_{ij} = \frac{mW(r_{ij}/h_i)}{h_i^3}, \quad (\text{B4})$$

with  $W(r_{ij}/h_i)$  given by

$$W(\mathbf{r}/h) = \frac{8}{\pi h^3} \begin{cases} 1 - 6\left(\frac{r}{h}\right)^2 + 6\left(\frac{r}{h}\right)^3, & 0 \leq \frac{r}{h} \leq \frac{1}{2}, \\ 2\left(1 - \frac{r}{h}\right)^3, & \frac{1}{2} < \frac{r}{h} \leq 1, \\ 0, & \frac{r}{h} > 1. \end{cases} \quad (\text{B5})$$

as used in GADGET I.  $m$  is the mass of the dark matter particles,  $r_{ij}$  is the distance between particle  $i$  and particle  $j$  and  $h_i$  the smoothing length of the dark matter particle.

In redshift space, a pixel at velocity  $v(k)$  suffers absorption from a pixel at velocity  $v(j)$  by an amount  $e^{-\tau(k)}$ , where  $\tau(k)$  is the contribution to the optical depth of bin  $k$  given by bin  $j$ :

$$\tau(k) = \frac{1}{\sqrt{\pi}} \sigma_\alpha \frac{c}{V_X(j)} n_X(j) a \Delta \cdot \exp \left\{ - \left[ \frac{v(k) - v(j)}{V_X(j)} \right]^2 \right\}. \quad (\text{B6})$$

The Doppler width  $V_X(j)$  of the species  $X$  with mass  $m_X$  determines the thermal broadening of the absorption lines. The Doppler width  $V_X(j)$  in pixel  $j$  is given by:

$$V_X^2(j) = \frac{2k_B T_X(j)}{m_X}, \quad (\text{B7})$$

where  $n_X(j)$  is the number density,  $T_X(j)$  the temperature in pixel  $j$  and  $c$  the speed of light. The Ly $\alpha$  cross section for H I is

$$\sigma_\alpha = \left( \frac{3\pi\sigma_T}{8} \right)^{1/2} f \lambda_\alpha = 4.45 \cdot 10^{-18} \text{ cm}^2, \quad (\text{B8})$$

with  $\lambda_\alpha = 1215.6 \text{ \AA}$  the rest wavelength of the transition and  $\sigma_T = 6.625 \cdot 10^{-25} \text{ cm}^2$  the Thomson cross section.  $f = 0.41615$  is the oscillator strength and measures the quantum mechanical departure from the classical harmonic oscillator.

We normalise our spectra by rescaling the mean flux ( $e^{-\tau_{\text{HI}}}$ ) to the mean flux measured in real spectra,  $e^{-\tau_{\text{eff}}}$ .  $\tau_{\text{HI}}$  is the H I opacity along our simulated LOS. The effective optical depth  $\tau_{\text{eff}}$  derived from observations is calculated as a function of redshift by using the relation between redshift and optical depth given by Kim et al. (2004) in Subsection 3.3 of their paper. The effective optical depth  $\tau_{\text{oss}}$  in our spectra is:

$$\tau_{\text{oss}} = -\ln(e^{-\tau_{\text{HI}}}). \quad (\text{B9})$$

With an iterative procedure we rescale  $\tau_{\text{oss}}$  to  $\tau_{\text{eff}}$  until the difference between the two is no larger than a few per cent, that is, typically,  $|\tau_{\text{oss}} - \tau_{\text{eff}}| < 0.005$ . This procedure allows us to make the artificial spectra directly comparable to the observed ones in each given redshift range. In addition, it somewhat washes out the dependence of the optical depth on the normalisation coefficient of the UV ionising background radiation  $J_{21}$ , which determines the ionisation fraction of hydrogen and therefore the absorption of the UV radiation.

## REFERENCES

- Adelberger K.L., Steidel C.C., Shapley A.E. & Pettini M., 2003, ApJ, 584, 45
- Adelberger K.L., Shapley A.E., Steidel C.C., Pettini M., Erb D.K. & Reddy N.A., 2005, ApJ, 629, 636 (A05)
- Bertone S., Stoehr F. & White S.D.M., 2005, MNRAS, 359, 1201 (BSW05)
- Bolton J.S., Haehnelt M.G., Viel M., Springel V., 2005, MNRAS, 357, 1178
- Cen R., 1992, ApJS, 78, 341
- Colless M. et al., 2001, MNRAS, 328, 1039
- Croft R.A.C., Weinberg D.H., Bolte M., Burles S., Hernquist L., Katz N., Kirkman D., Tytler D., 2002, ApJ, 581, 20
- Croft R.A.C., Weinberg D.H., Katz N., Hernquist L., 1998, ApJ, 495, 44
- Desjacques V., Nusser A., Haehnelt M.G., Stoehr F., 2004, MNRAS, 350, 879
- Fang T., Loeb A., Tytler D., Kirkman D., Suzuki N., 2005, pre-print astro-ph/0505182
- Haardt F., Madau P., Rees M.J., 1999, ApJ, 514, 648
- Haardt F., Madau P., 1996, ApJ, 461 20
- Hoopes C.G., Heckman T.M., Strickland D.K. & Howk J.C., 2003, ApJL, 596, 175
- Hui L., Burles S., Seljak U., Rutledge R.E., Magnier E., Tytler D., 2001, ApJ, 552, 15
- Hui L., Gnedin N.Y., 1997, MNRAS, 292, 27
- Kim T.-S., Viel M., Haehnelt M.G., Carswell R. F., Cristiani S., 2004, MNRAS, 347, 355
- Kollmeier J.A., Weinberg D.H., Davé R., Katz N., 2003, ApJ, 594, 75
- Lidz A., Heitmann K., Hui L., Habib S., Rauch M., Sargent W.L.W., 2005, pre-print astro-ph/0505138
- Maselli A., Ferrara A., Bruscoli M., Marri S., Schneider R., 2004, MNRAS, 350, 21
- McDonald P., Seljak U., Burles S., Schlegel D.J., Weinberg D.H., Shih D., Schaye J., Schneider D.P., Brinkmann J., Brunner R.J., Fukugita M., 2004, pre-print astro-ph/0405013
- McDonald P., Seljak U., Cen R., Bode P., Ostriker J.P., 2005, MNRAS, 360, 1471
- McDonald P., Miralda-Escudé J., Rauch M., Sargent W.L.W., Barlow T.A., Cen R., Ostriker J.P., 2000, ApJ, 543, 1
- Ostriker J.P. & McKee C.F., 1988, Rev.Mod.Phys. 60, 1
- Rupke D.S., Veilleux S., Sanders D.B., 2005, pre-print astro-ph/0507037.
- Schaye J., Theuns T., Rauch M., Efstathiou G., Sargent W.L.W., 2000, MNRAS, 318, 817
- Shapley A.E., Steidel C.C., Pettini M. & Adelberger K.L., 2003, ApJ, 588, 65
- Spergel D.N., Verde L., Peiris H.V., Komatsu E., Nolte M.R., Bennett, C.L., Halpern M., Hinshaw G., Jarosik N., Kogut A., Limon M., Meyer S.S., Page L., Tucker G.S., Weiland J.L., Wollack E., Wright E.L., 2003, ApJS, 148, 175
- Springel V., Yoshida N. & White S.D.M., 2001a, New Astronomy, 6, 79
- Springel V., White S.D.M., Tormen G. & Kauffmann G., 2001b, MNRAS, 328, 726
- Stoehr F., 2003, PhD Thesis, Ludwig Maximilian Univer-

sität, München

Strickland D.K. & Stevens I.R., 2000, MNRAS, 314, 511

Tegmark M. et al, 2004, ApJ, 606, 702

Theuns T., Leonard A., Efstathiou G., Pearce F.R.,  
Thomas P.A., 1998, MNRAS, 301, 478

Viana P.T.P., Nichol R.C., Liddle A.R., 2002, ApJ, 569, 75

Viel M., Weller J. & Haehnelt M.G., 2004a, MNRAS, 355,  
23

Viel M., Haehnelt M.G. & Springel V., 2004b, MNRAS,  
354, 684

Viel M., Haehnelt M.G., Carswell R.F., Kim T.-S., 2004c,  
MNRAS, 349, 33

White S.D.M., Frenk C.S., 1991, ApJ, 379, 52

This paper has been typeset from a  $\text{\TeX}$ / $\text{\LaTeX}$  file prepared  
by the author.